Available online at www.sciencedirect.com
SCIENCE DIRECT®
Journal of Magnetic Resonance 169 (2004) 225–239
JMR Journal of Magnetic Resonance
www.elsevier.com/locate/jmr

Simple modeling of dipolar coupled ^{7}Li spins and stimulated-echo spectroscopy of single-crystalline β-eucryptite

F. Qi,[a,b] G. Diezemann,[b] H. Böhm,[c] J. Lambert,[d] and R. Böhmer[a,*]

[a] *Experimentelle Physik III, Universität Dortmund, 44221 Dortmund, Germany*
[b] *Institut für Physikalische Chemie, Johannes Gutenberg-Universität, 55099 Mainz, Germany*
[c] *Institut für Geowissenschaften, Johannes Gutenberg-Universität, 55099 Mainz, Germany*
[d] *Institute for Analytical Sciences (ISAS), 44139 Dortmund, Germany*

Received 22 January 2004; revised 21 April 2004
Available online 5 June 2004

Abstract

Stimulated-echo spectroscopy has recently been applied to study the ultra-slow dynamics of nuclear spin-3/2 probes such as ^{7}Li and ^{9}Be in solids. Apart from the dominant first-order quadrupolar interaction in the present article also the impact of the homonuclear dipolar interactions is considered in a simple way: the time evolution of a dipole coupled pair of spins with $I = 3/2$ is calculated in an approximation, which takes into account that the satellite transitions usually do not overlap. Explicit analytical expressions describing various aspects of a coupled quadrupolar pair subjected to a Jeener–Broekaert pulse sequence are derived. Extensions to larger spin systems are also briefly discussed. These results are compared with experimental data on a single-crystalline Li ion conductor.

Keywords: Nuclear magnetic resonance; Quadrupolar nuclei; Dipolar interactions; Stimulated spin echoes; Ion transport

1. Introduction

Stimulated-echo spectroscopy is a powerful method to unravel details of the slow dynamical processes in organic as well as in inorganic solids. Spin-1/2 and spin-1 nuclei have long been used for this purpose, see, e.g. [1]. But with a few exceptions [2] spin-3/2 nuclei governed by first-order quadrupolar shifts have only recently been considered in this context [3,4]. Here the Jeener–Broekaert sequence [5] was applied to ^{9}Be and ^{7}Li species in metallic glasses, ferroelectrics, and ion conductors [6,7]. For ^{9}Be it is a good approximation to consider that the quadrupolar interactions dominate the systematic time evolution of the spin system. However, ^{7}Li has a much larger gyromagnetic ratio and the dipolar interactions are typically 7–8 times stronger than for ^{9}Be. Consequently, for static samples it turned out to be possible to generate pure quadrupolar ^{9}Be spin-alignment states, while for ^{7}Li this could not be achieved so far for isotopically undiluted samples [8]. A pure quadrupolar spin-alignment state in a solid is associated with a symmetrically split spectrum devoid of any central features. The appearance of the latter in ^{7}Li stimulated-echo spectra was ascribed to the impact of homonuclear dipolar interactions [8].

A detailed description of a spin-3/2 system in the presence of dipolar interactions is not available at present. However, a more quantitative understanding of the systematic time evolution is needed for a more detailed interpretation of the spectroscopy of the slow Li ion hopping using the stimulated-echo technique. It is the goal of this work to contribute to a more quantitative theoretical description of the homonuclear dipolar interactions between ^{7}Li-spins. In the experimental part of present article we focus on the effect of these interactions on spectra and on two-time correlation functions. However, our results may also be important when studying higher-order correlation functions in Li ion

* Corresponding author. Fax: +49-231-755-3516.
E-mail address: Roland.Bohmer@uni-dortmund.de (R. Böhmer).

1090-7807/$ - see front matter © 2004 Elsevier Inc. All rights reserved.
doi:10.1016/j.jmr.2004.04.018

conductors, a subject that was recently addressed using molecular dynamics simulations [9].

Homonuclear dipolar interactions were also found to be an important feature in some ion conductors in which the ^{7}Li probes predominantly evolve under the action of transferred hyperfine fields [10]. Here the dipolar interactions were reported to lead to unwanted cross-peaks in two-dimensional exchange spectra [11]. However, using rapid sample spinning the adverse effect of the dipolar interactions among the ^{7}Li spins could be suppressed. The time evolution of homo- and heteronuclear couplings among spins $I \geqslant 3/2$ in rotating solids, particularly that under the action of a dominant second-order quadrupolar Hamiltonian, has been the subject of numerous investigations, e.g. [12]. Although the thermodynamics of dipolar coupled many-body systems were extensively dealt with [13] the explicit time evolution of the much simpler case of a pair of dipolar coupled 3/2 spins, subject to first-order quadrupolar perturbations, to our knowledge was not treated, so far. For spin-1/2 pairs the corresponding problem is of course solved, see, e.g. [14], and this is also true for spin-1 nuclei [15–19], here referring to static (non-rotating) samples.

It is therefore the main purpose of the present article to give a simple, mostly analytic description of a dipolar coupling between a pair of ^{7}Li-spins systematically evolving under a stronger secular quadrupolar Hamiltonian. To start with we diagonalize the corresponding Hamilton operator. Then we focus the discussion on a reduced Hamiltonian in which only elements involving the central transitions are retained. This simple approximation is motivated by the fact that in a crystal with a complex structure or in an amorphous solid the satellite transitions of adjacent ^{7}Li spins may be expected to differ energetically. Then within the product operator formalism the time evolution for a Jeener–Broekaert type of experiment is calculated. Heteronuclear dipole and chemical shift interactions are not considered in these computations since the Jeener–Broekaert echo should refocus them.

To test some aspects of these calculations and as part of our program devoted to the investigation of solid-state electrolytes [7,8], we studied single crystals of β-eucryptite ($LiAlSiO_4$). This quasi-one-dimensional Li^+ ion conductor was extensively studied in the past by ^{7}Li-NMR, mostly focusing on spin–lattice relaxation times and absorption spectra [20–23]. From rotation patterns the maximum separation of the quadrupolar satellites was found to be about 130 kHz [24] and the width of the central line ranged from about 4 to 6 kHz [25]. Various other methods including X-ray [26] and neutron diffraction [27–30], as well as impedance spectroscopy on single crystals [31–33] and on polycrystalline samples [34,35] were applied to this aluminosilicate.

At high temperatures β-eucryptite exhibits a stuffed hexagonal high-quartz (β-SiO_2) structure which on the average corresponds to the space group $P6_222$. At $T = 755$ K which is larger than the highest temperature studied in this article an order–disorder transition involving the Li ions takes place. Otherwise the structure is made up from helically connected SiO_4 and AlO_4 tetrahedra. This arrangement gives rise to two structurally distinguishable channels along the c axis in which the charge compensating Li^+ ions are located. In each channel 3 magnetically inequivalent sites exist, which are all coordinated by 4 oxygen atoms. The ionic motion within each channel is fast as compared to the inter-channel dynamics. Consequently the electrical conductivity is strongly anisotropic. Interestingly this is also true for the thermal expansion: while along the *c*-direction the linear expansion coefficient is negative, those perpendicular to the *c*-axis are positive. The resulting negative thermal *volume* expansion coefficient is the basis for numerous technological applications [36].

This paper is organized as follows. First, we derive the energy level diagram for a pair of dipolar coupled spin-3/2 and for the case of coupling among magnetically inequivalent spins give the diagonal part of the density matrix that can be generated using two pulses that are out of phase. Considering the Jeener–Broekaert sequence on the basis of these computations we evaluate (i) the dependence on the acquisition time or the corresponding spectra (Section 2.1) and (ii) the dependence on the mixing time in the echo variant of the experiment (Section 2.2). Then in Section 2.3 we consider generalizations of our approach to spin-triples and powder averages. These calculations form the basis for the interpretation of the experimental results of the ion conductor β-eucryptite that we present in Section 3. In turn we deal with the spectra (Section 3.1), the dependence on the evolution time (Section 3.2), and the dependence on the mixing time (Section 3.3) using the spin-alignment or Jeener–Broekaert echo. Finally, in Section 4 we discuss the temperature dependence of the time constants derived from these experiments and conclude in Section 5.

2. Spin-alignment of coupled ^{7}Li pairs

To prepare for the discussion of dipolar coupled spin-3/2 nuclei evolving under the quadrupolar interaction we will first consider an isolated spin *i* in a large Zeeman field

$$\hat{H}_z^{(i)} = \omega_L^{(i)} \hat{I}_z^{(i)} = \omega_L^{(i)} \hat{T}_{10}^{(i)}. \tag{1}$$

We use the normalized spherical tensor operators $\hat{T}_{lm}^{(i)}$, see, e.g. [37]. The first-order Hamiltonian in the rotating frame

$$\hat{H}_Q^{(i)} = \frac{\omega_{Qi}}{6}(3\hat{I}_z^{(i)}\hat{I}_z^{(i)} - I(I+1)) = \omega_{Qi}\hat{T}_{20}^{(i)}, \tag{2}$$

can be employed to generate a pure spin-alignment state $\hat{T}_{20}$ by a cycle of two properly phased RF pulses [38]. A possible phase cycle employing X- and Y-pulses is shown in Table 1. During the evolution time t_p separating the two pulses with flip angles φ_1 and φ_2 the alignment state acquires an amplitude modulation which can be expressed by a factor $\sin(\omega_{Qi}t_p)$ with $\omega_{Qi} = \frac{1}{2}\delta_Q^{(i)}(3\cos^2\theta_Q^{(i)} - 1 - \eta^{(i)}\sin^2\theta_Q^{(i)}\cos 2\phi_Q^{(i)})$ and $\delta_Q^{(i)} = \frac{1}{2}\frac{eqeQ}{\hbar}$ for $I = 3/2$. Here the symbols have their usual meaning. After a mixing time t_m a third pulse can be used to generate a two-time autocorrelation function. The Jeener–Broekaert sequence used for this study can thus be described by $X_{\varphi 1}$–t_p–$Y_{\varphi 2}$–t_m–$X_{\varphi 3}$–t_p-acquisition.

The flip angles $\varphi_1 = 90°$, $\varphi_2 = 45°$, and $\varphi_3 = 45°$ maximize the alignment signal [4]

$$S_2^{(i)}(t_p, t_m, t) = \frac{9}{20}\sin(\omega_{Qi}(0)t_p)\sin(\omega_{Qi}(t_m)t), \tag{3}$$

which via

$$\sin(\omega_Q t_p)\sin(\omega_Q t) = \frac{1}{2}[\cos(\omega_Q t_p - \omega_Q t) - \cos(\omega_Q t_p + \omega_Q t)], \tag{4}$$

can be decomposed into an echo-part showing up for $t = t_p$ and a transient (or anti-echo) part. The Fourier spectrum with respect to the detection time t thus gives a pair of lines at $\pm\omega_{Qi}$.

Next we will turn to incorporate also the homonuclear dipole coupling which yields the laboratory frame operator

$$\hat{H}_{lab}^{(i,j)} = \hat{H}_Z^{(i,j)} + \hat{H}_Q^{(i,j)} + \hat{H}_D^{(i,j)}. \tag{5}$$

Chemical shift interactions are not included in this expression (i) because they are quite small for the application we have in mind (^{7}Li-NMR) and (ii) because they will be refocused by the Jeener–Broekaert sequence that we use as a basis for the computations and experiments in this article. At the lowest fields used in this study second-order quadrupolar effects should be of the order of $\left(\frac{1}{12} + \frac{3}{64}\right)\frac{\omega_Q^2}{\omega_L} = 2\pi \times 0.13\,\frac{130^2}{46{,}000}\,\text{kHz} \approx 2\pi \times 48\,\text{Hz}$ [39] and therefore considerably smaller than the dipolar and first-order quadrupolar interactions. These are of the order of 5 and 130 kHz, respectively. Therefore in the present article no second-order quadrupolar effects will be considered.

Table 1
A 32-fold phase cycle can be obtained by combining the phases of pulses with flip angles φ_1 and φ_2 given in the table with the detection pulses +X, −X, +Y, and −Y

No.	φ_1	φ_2	Receiver
1	+X	+Y	−
2	−X	+Y	+
3	+X	−Y	+
4	−X	−Y	−
5	+Y	+X	+
6	−Y	+X	−
7	+Y	−X	−
8	−Y	−X	+

The resulting cycle was assumed as the basis for the computations and used in the experimental implementation.

Below, the operators appearing in Eq. (5) will be expressed using the tensor product $\hat{T}_{lm}^{(i)}\hat{T}_{l'm'}^{(j)} = \hat{T}_{lm}^{(i)} \otimes \hat{T}_{l'm'}^{(j)}$ also including the unity operator $\hat{T}_{00}$. This means that in addition to the Zeeman term

$$\hat{H}_Z^{(i,j)} = \omega_L^{(i)}\hat{T}_{10}^{(i)}\hat{T}_{00}^{(j)} + \omega_L^{(j)}\hat{T}_{00}^{(i)}\hat{T}_{10}^{(j)}, \tag{6}$$

and the quadrupolar term

$$\hat{H}_Q^{(i,j)} = \omega_Q^{(i)}\hat{T}_{20}^{(i)}\hat{T}_{00}^{(j)} + \omega_Q^{(j)}\hat{T}_{00}^{(i)}\hat{T}_{20}^{(j)}, \tag{7}$$

the homonuclear dipolar interaction

$$\hat{H}_D^{(i,j)} = \omega_d^{(i,j)}(2\hat{I}_z^{(i)}\hat{I}_z^{(j)} - \frac{1}{2}(\hat{I}_i^+\hat{I}_j^- + \hat{I}_i^-\hat{I}_j^+)) \propto \hat{T}_{20}^{(i,j)}, \tag{8}$$

for a spin pair (i, j) will be considered. In the latter expression the coupling frequency

$$\omega_d^{(i,j)} = -\frac{\mu_0}{4\pi}\hbar\frac{\gamma^2}{r_{ij}^3}\frac{1}{2}(3\cos^2\theta_{ij} - 1), \tag{9}$$

appears. The total operator of the system is then obtained by summing over all spin pairs. However, as a simple approach here we will focus on just a pair of spins to obtain insight into the problem by analytical

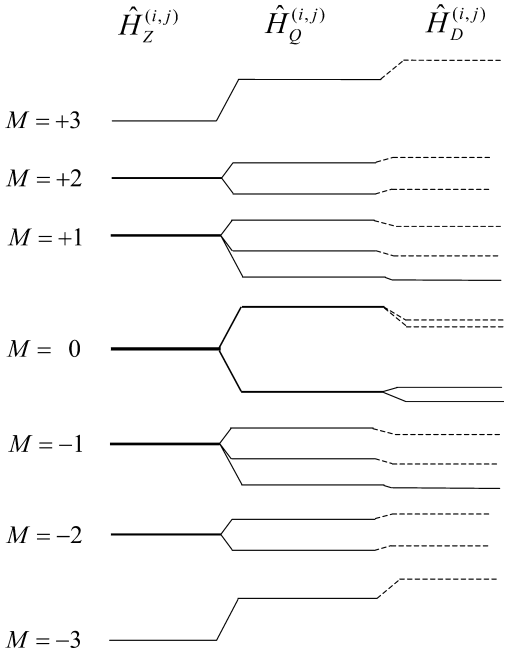

Fig. 1. Schematic representation of the energy level diagram of a dipolar coupled spin-3/2 pair resulting from the diagonalization of $\hat{H}_{lab}^{(i,j)}|m_i, m_j\rangle = E_M|m_i, m_j\rangle$, i.e., Eq. (10). Here m_i and m_j denote the quantum numbers of spins i and j, respectively. The various contributions to the Hamiltonian $\hat{H}_{lab}^{(i,j)} = \hat{H}_Z^{(i,j)} + \hat{H}_Q^{(i,j)} + \hat{H}_D^{(i,j)}$ are those summarized in Eq. (5). The energies E_M are shown for the possible values of the total magnetic quantum number $M = m_i + m_j$ that runs from −3 to +3. The level spacing shown corresponds roughly to $\omega_L^{(i)} = \omega_L^{(j)}$ and $\omega_{Qi} = 2\omega_{Qj} = 10\omega_D$.

Table 2
Energies E_M obtained from the solution of Eq. (10)

M	$\hat{H}_{\text{lab}}^{(i,j)}$	$\hat{H}_{\text{app}}^{(i,j)}$
+3	$+3\omega_L+\alpha$	$+3\omega_L+\Sigma/2$
+2	$+2\omega_L+\beta_{+1}$	$+2\omega_L+\Delta/2$
	$+2\omega_L+\beta_{-1}$	$+2\omega_L-\Delta/2$
+1	$+\omega_L+\gamma_0$	$+\omega_L+\Delta/2$
	$+\omega_L+\gamma_2$	$+\omega_L-\Delta/2$
	$+\omega_L+\gamma_1$	$+\omega_L-(\Sigma-\omega_D)/2$
0	δ_{+1}	$+\Sigma/2$
	ε_{+1}	$+\Sigma/2$
	δ_{-1}	$-\Sigma/2+3\omega_D/2$
	ε_{-1}	$-\Sigma/2-5\omega_D/2$
−1	$-\omega_L+\gamma_0$	$-\omega_L+\Delta/2$
	$-\omega_L+\gamma_2$	$-\omega_L-\Delta/2$
	$-\omega_L+\gamma_1$	$-\omega_L-(\Sigma-\omega_D)/2$
−2	$-2\omega_L+\beta_{+1}$	$-2\omega_L+\Delta/2$
	$-2\omega_L+\beta_{-1}$	$-2\omega_L-\Delta/2$
−3	$-3\omega_L+\alpha$	$-3\omega_L+\Sigma/2$

Analytical expressions for the coefficients α through ε are given in Eq. (11). The order in which these coefficients appear in this table corresponds to the order of levels used in Fig. 1.

calculations. The energy levels E_M resulting from the diagonalization of the Hamiltonian given by Eq. (5)

$$\hat{H}_{\text{lab}}^{(i,j)}|m_i,m_j\rangle = E_M|m_i,m_j\rangle \tag{10}$$

$$\gamma_k = \frac{1}{6}\left(k_0 + 4k_1^{1/6}\cos\left(\frac{1}{3}\left(2\pi k + \arccos\left(\frac{k_2}{2\sqrt{k_1}}\right)\right)\right)\right),$$
$$k = 0,1,2,$$

with $k_0 = -\Sigma - 5\omega_D$,
$$k_1 = (22\omega_D^2 - 2\omega_D\Sigma + \Delta^2 + \omega_{Qi}\omega_{Qj})^3$$
$$k_2 = (4\omega_D - \Sigma)(31\omega_D^2 - 2\omega_D\Sigma - 2\Delta^2 + \omega_{Qi}\omega_{Qj}), \tag{11}$$

$$\delta_{\pm1} = \frac{1}{2}(-3\omega_D \pm \sqrt{\Sigma^2 - 12\omega_D\Sigma + 45\omega_D^2}),$$

$$\varepsilon_{\pm1} = \frac{1}{2}(-7\omega_D \pm \sqrt{\Sigma^2 - 4\omega_D\Sigma + 13\omega_D^2}),$$

with $\Sigma = \omega_{Qi} + \omega_{Qj}$

and $\Delta = \omega_{Qi} - \omega_{Qj}$.

With the selection rule $\Delta M = \pm 1$ the transition frequencies as given by the energy level diagram thus defined (see also Fig. 1) are $\omega_Q + n\omega_D$ with $n = 0, +1, \pm 3$.

The dipolar and the quadrupolar contributions to the rotating frame operator

$$\hat{H}_{\text{rot}}^{(i,j)} = \hat{H}_Q^{(i,j)} + \hat{H}_D^{(i,j)}$$
$$= \frac{1}{2}\begin{bmatrix}
\Sigma+9\omega_D & 0 & 0 & 0 & 0 & 0 & 0 & 0 & 0 & 0 & 0 & 0 & 0 & 0 & 0 & 0 \\
0 & \Delta+3\omega_D & 0 & 0 & -3\omega_D & 0 & 0 & 0 & 0 & 0 & 0 & 0 & 0 & 0 & 0 & 0 \\
0 & 0 & \Delta-3\omega_D & 0 & 0 & -2\sqrt{3}\omega_D & 0 & 0 & 0 & 0 & 0 & 0 & 0 & 0 & 0 & 0 \\
0 & 0 & 0 & \Sigma-9\omega_D & 0 & 0 & -3\omega_D & 0 & 0 & 0 & 0 & 0 & 0 & 0 & 0 & 0 \\
0 & -3\omega_D & 0 & 0 & -\Delta+3\omega_D & 0 & 0 & 0 & 0 & 0 & 0 & 0 & 0 & 0 & 0 & 0 \\
0 & 0 & -2\sqrt{3}\omega_D & 0 & 0 & \boxed{-\Sigma+\omega_D} & 0 & 0 & -2\sqrt{3}\omega_D & 0 & 0 & 0 & 0 & 0 & 0 & 0 \\
0 & 0 & 0 & -3\omega_D & 0 & 0 & \boxed{-\Sigma-\omega_D} & 0 & 0 & \boxed{-4\omega_D} & 0 & 0 & 0 & 0 & 0 & \\
0 & 0 & 0 & 0 & 0 & 0 & 0 & -\Delta-3\omega_D & 0 & 0 & -2\sqrt{3}\omega_D & 0 & 0 & 0 & 0 & 0 \\
0 & 0 & 0 & 0 & 0 & -2\sqrt{3}\omega_D & 0 & 0 & -\Delta-3\omega_D & 0 & 0 & 0 & 0 & 0 & 0 & 0 \\
0 & 0 & 0 & 0 & 0 & 0 & \boxed{-4\omega_D} & 0 & 0 & \boxed{-\Sigma-\omega_D} & 0 & 0 & -3\omega_D & 0 & 0 & 0 \\
0 & 0 & 0 & 0 & 0 & 0 & 0 & -2\sqrt{3}\omega_D & 0 & 0 & \boxed{-\Sigma+\omega_D} & 0 & 0 & -2\sqrt{3}\omega_D & 0 & 0 \\
0 & 0 & 0 & 0 & 0 & 0 & 0 & 0 & 0 & 0 & 0 & -\Delta+3\omega_D & 0 & 0 & -3\omega_D & 0 \\
0 & 0 & 0 & 0 & 0 & 0 & 0 & 0 & 0 & -3\omega_D & 0 & 0 & \Sigma-9\omega_D & 0 & 0 & 0 \\
0 & 0 & 0 & 0 & 0 & 0 & 0 & 0 & 0 & 0 & -2\sqrt{3}\omega_D & 0 & 0 & \Delta-3\omega_D & 0 & 0 \\
0 & 0 & 0 & 0 & 0 & 0 & 0 & 0 & 0 & 0 & 0 & -3\omega_D & 0 & 0 & \Delta+3\omega_D & 0 \\
0 & 0 & 0 & 0 & 0 & 0 & 0 & 0 & 0 & 0 & 0 & 0 & 0 & 0 & 0 & \Sigma+9\omega_D
\end{bmatrix} \tag{12}$$

with $M = m_i + m_j$ and $M = 3,2,1,0,-1,-2,-3$ is sketched in Fig. 1 for $\omega_L^{(i)} = \omega_L^{(j)}$ and a particular choice of dipolar and quadrupolar precession frequencies. The energies E_M, compiled in Table 2, involve the following abbreviations:

$$\alpha = \frac{\Sigma}{2} + \frac{9\omega_D}{2},$$

$$\beta_{\pm1} = \pm\frac{\sqrt{\Delta^2 + 9\omega_D^2}}{2} + \frac{3\omega_D}{2},$$

here represented in the product basis $|m_i,m_j\rangle$ of the Zeeman eigenstates do not commute with one another. This is due to the fact that the overall quadrupolar alignment state implicit in Eq. (7) is not invariant under the flip-flop term $\hat{I}_i^+\hat{I}_j^- + \hat{I}_i^-\hat{I}_j^+ \propto \hat{T}_{11}^{(i)}\hat{T}_{1-1}^{(j)} + \hat{T}_{1-1}^{(i)}\hat{T}_{11}^{(j)}$ of the dipolar Hamiltonian, Eq. (8). This can be remedied by treating the dipolar interaction in a particular fashion, i.e., by setting $\omega_D = 0$, except for those matrix elements involving the central levels of the energy scheme depicted in Fig. 2. These elements are specifically marked in Eq. (12). The resulting approximate Hamiltonian will be denoted as

$$\hat{H}^{(i,j)}_{\mathrm{app}} = \frac{1}{2}\begin{bmatrix}
\Sigma & 0 & 0 & 0 & 0 & 0 & 0 & 0 & 0 & 0 & 0 & 0 & 0 & 0 & 0 & 0\\
0 & \Delta & 0 & 0 & 0 & 0 & 0 & 0 & 0 & 0 & 0 & 0 & 0 & 0 & 0 & 0\\
0 & 0 & \Delta & 0 & 0 & 0 & 0 & 0 & 0 & 0 & 0 & 0 & 0 & 0 & 0 & 0\\
0 & 0 & 0 & \Sigma & 0 & 0 & 0 & 0 & 0 & 0 & 0 & 0 & 0 & 0 & 0 & 0\\
0 & 0 & 0 & 0 & -\Delta & 0 & 0 & 0 & 0 & 0 & 0 & 0 & 0 & 0 & 0 & 0\\
0 & 0 & 0 & 0 & 0 & -\Sigma+\omega_D & 0 & 0 & 0 & 0 & 0 & 0 & 0 & 0 & 0 & 0\\
0 & 0 & 0 & 0 & 0 & 0 & -\Sigma-\omega_D & 0 & 0 & -4\omega_D & 0 & 0 & 0 & 0 & 0 & 0\\
0 & 0 & 0 & 0 & 0 & 0 & 0 & -\Delta & 0 & 0 & 0 & 0 & 0 & 0 & 0 & 0\\
0 & 0 & 0 & 0 & 0 & 0 & 0 & 0 & -\Delta & 0 & 0 & 0 & 0 & 0 & 0 & 0\\
0 & 0 & 0 & 0 & 0 & 0 & -4\omega_D & 0 & 0 & -\Sigma-\omega_D & 0 & 0 & 0 & 0 & 0 & 0\\
0 & 0 & 0 & 0 & 0 & 0 & 0 & 0 & 0 & 0 & -\Sigma+\omega_D & 0 & 0 & 0 & 0 & 0\\
0 & 0 & 0 & 0 & 0 & 0 & 0 & 0 & 0 & 0 & 0 & -\Delta & 0 & 0 & 0 & 0\\
0 & 0 & 0 & 0 & 0 & 0 & 0 & 0 & 0 & 0 & 0 & 0 & \Sigma & 0 & 0 & 0\\
0 & 0 & 0 & 0 & 0 & 0 & 0 & 0 & 0 & 0 & 0 & 0 & 0 & \Delta & 0 & 0\\
0 & 0 & 0 & 0 & 0 & 0 & 0 & 0 & 0 & 0 & 0 & 0 & 0 & 0 & \Delta & 0\\
0 & 0 & 0 & 0 & 0 & 0 & 0 & 0 & 0 & 0 & 0 & 0 & 0 & 0 & 0 & \Sigma
\end{bmatrix}. \quad (13)$$

Since the only non-vanishing off-diagonal elements are $\langle -\frac{1}{2}, +\frac{1}{2}|\hat{H}^{(i,j)}_{\mathrm{app}}|+\frac{1}{2}, -\frac{1}{2}\rangle = \langle +\frac{1}{2}, -\frac{1}{2}|\hat{H}^{(i,j)}_{\mathrm{app}}|-\frac{1}{2}, +\frac{1}{2}\rangle = -4\omega_D$ this matrix can easily be transformed into diagonal form yielding the eigenvalues given in the third column of Table 2. The resulting level scheme is thus similar to the one depicted in Fig. 1.

The approximation implicit in $\hat{H}^{(i,j)}_{\mathrm{app}}$ appears well justified if the quadrupolar frequencies are sufficiently different, so that the flip-flop processes which involve the outer levels become suppressed since they would violate energy conservation. Due to the strong distance dependence implicit in Eq. (9) a difference in the quadrupolar frequencies means that neighboring and possibly next-neighboring sites should not be magnetically equivalent. This criterion is automatically, practically always fulfilled in amorphous materials. It is obviously not valid for crystals in general, but it applies to β-eucryptite, i.e., for the one dimensional conductor studied in the experimental part of this work. In β-eucryptite the minimum distance between two adjacent, magnetically inequivalent Li ions is about 3.73 Å and the smallest separation between magnetically equivalent sites within each channel is three time larger [26].

Since $[\hat{H}^{(i,j)}_{\mathrm{app}}, \hat{H}^{(i,j)}_{Q}] = 0$, the overall quadrupolar alignment state is invariant under the approximate Hamiltonian. Therefore, during the mixing time this state is well suited to store the amplitude modulation acquired by the dipolar coupled quadrupolar spin pair in the course of the evolution period. Starting from the initial density matrix, $\rho(0) = \hat{T}^{(i)}_{10}\hat{T}^{(j)}_{00} + \hat{T}^{(i)}_{00}\hat{T}^{(j)}_{10}$, the application of RF pulses is easily computed via the rotating frame operator which, e.g., for an X-pulse reads $\hat{H}^{(i,j)}_{x} = \omega_1(\hat{I}^{(i)}_{x} \otimes \hat{T}^{(j)}_{00} + \hat{T}^{(i)}_{00} \otimes \hat{I}^{(j)}_{x})$. Employing the phase cycle referred to in the previous section, immediately after the second pulse we obtain a density matrix $\rho(t_{\mathrm{p}})$ which contains diagonal and off-diagonal elements. The latter correspond to multiple quantum (MQ) coherences

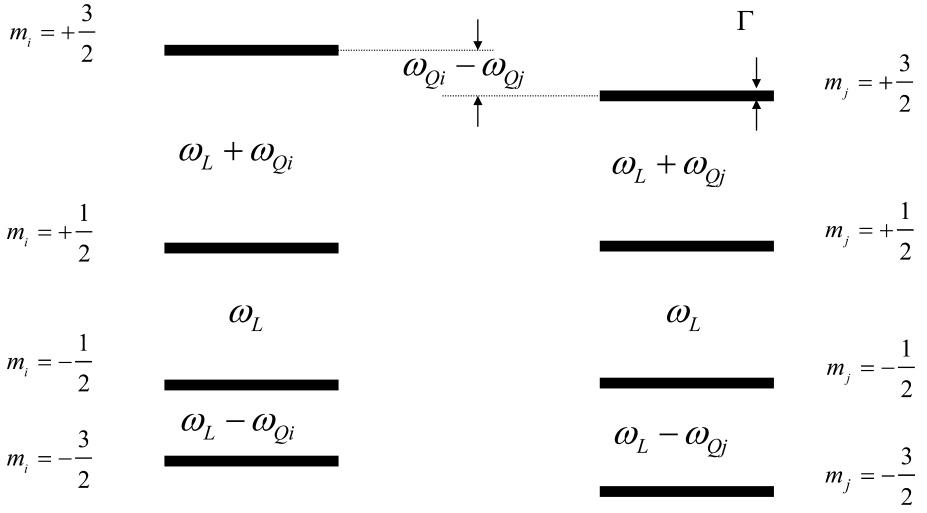

Fig. 2. Energy level scheme of two isolated spins with $I = 3/2$. The bars are meant to indicate the dipolar broadening of the levels by a width Γ.

that will dephase in the subsequent mixing time. The diagonal part of $\rho(t_p)$ can be decomposed into the following structure:

$$\rho_{dia}(t_p) = c_{11}\hat{T}_{10}\hat{T}_{10} + c_{02}\hat{T}_{00}\hat{T}_{20} + c_{20}\hat{T}_{20}\hat{T}_{00} + c_{13}\hat{T}_{10}\hat{T}_{30} + c_{31}\hat{T}_{30}\hat{T}_{10} + c_{22}\hat{T}_{20}\hat{T}_{20} + c_{33}\hat{T}_{30}\hat{T}_{30}, \quad (14)$$

where the indices i and j have been dropped. Thus only terms with *even* $L = l_i + l_j$ and $m_i = m_j = 0$ appear. As an aside we remark that a sequence of two RF pulses which are in phase yield a density matrix with diagonal elements which can be written as a linear combination of terms with *odd* L. Analytical expressions for all coefficients $c_{l_i l_j} = c_{l_i l_j}(t_p)$, which contain the encoding by the quadrupolar and the dipolar frequencies are given elsewhere [40].

Starting from Eq. (14) we may ask whether relaxation effects will give rise to additional terms. Following the treatment of [37,41,42] it is easy to see that quadrupolar relaxation does not lead to the appearance of contributions not already contained in that equation. Quadrupolar relaxation merely rescales the amplitudes of the individual product operators appearing in that expression.

2.1. Spectra

By Fourier transforming the $c_{l_i l_j}(t_p)$ coefficients with respect to t_p we can obtain the corresponding spectra $C_{ij}(\omega)$. These are associated with the tensor products $\hat{T}_{l_i 0}\hat{T}_{l_j 0}$ for given values of coupling frequencies. If l_1 and l_2 are both even then no central components are present, but of course a central component is present when both are odd, cf. Fig. 3.

Each of the seven terms appearing in Eq. (14) commutes with $\hat{H}^{(i,j)}_{app}$. The signal appearing after the application of the third pulse can therefore be computed in a straightforward manner from that equation. The result can written as a sum of 9 terms

$$\begin{aligned} S_2^{(i,j)}(t_p, t_m, t) = {} & a_{\omega_{Qi}}\sin(\omega_{Qi}t) + a_{\omega_{Qj}}\sin(\omega_{Qj}t) \\ & + a_{3\omega_D}\sin(3\omega_D t) + b_{\omega_{Qi}}\sin\left(\left(\frac{\omega_D}{2} - \omega_{Qi}\right)t\right) \\ & + b_{\omega_{Qj}}\sin\left(\left(\frac{\omega_D}{2} - \omega_{Qj}\right)t\right) \\ & + b_{3\omega_{Qi}}\sin\left(\left(\frac{3\omega_D}{2} - \omega_{Qi}\right)t\right) \\ & + b_{3\omega_{Qj}}\sin\left(\left(\frac{3\omega_D}{2} - \omega_{Qj}\right)t\right) \\ & + b_{5\omega_{Qi}}\sin\left(\left(\frac{5\omega_D}{2} + \omega_{Qi}\right)t\right) \\ & + b_{5\omega_{Qj}}\sin\left(\left(\frac{5\omega_D}{2} + \omega_{Qj}\right)t\right). \end{aligned} \quad (15)$$

The amplitude modulation of the signal written out in Eq. (15) is given by the a and b terms which depend on the evolution time t_p. Consequently they can in turn be written as linear combinations of the coefficients $c_{l_i l_j}$, e.g., $a_{\omega_{Qi}} = \frac{3}{80}(4\sqrt{6}c_{20} + 3c_{22})$. Fourier transformation of the $a(t_p)$ and $b(t_p)$ functions with respect to t_p yields the associated spectra $A(\omega)$ and $B(\omega)$ which in general contain 9 pairs of lines at $\pm\omega_{Qi}$, $\pm\omega_{Qj}$, $\pm 3\omega_D$, etc. Some examples are shown in Fig. 4. For all terms containing quadrupolar modulations, the peaks at the quadrupolar frequencies dominate. On the other hand, the coefficient

$$\begin{aligned} a_{3\omega_D} = \frac{1}{20,480}\Bigg\{ & 292\sin(3\omega_D t_p) + 3\Bigg[-5\sin\left(\left(\frac{\omega_D}{2} - \omega_{Qi}\right)t_p\right) - 5\sin\left(\left(\frac{\omega_D}{2} - \omega_{Qj}\right)t_p\right) \\ & + 22\sin\left(\left(\frac{3\omega_D}{2} - \omega_{Qi}\right)t_p\right) \\ & + 22\sin\left(\left(\frac{3\omega_D}{2} - \omega_{Qj}\right)t_p\right) \\ & + 17\sin\left(\left(\frac{5\omega_D}{2} + \omega_{Qi}\right)t_p\right) \\ & + 17\sin\left(\left(\frac{5\omega_D}{2} + \omega_{Qj}\right)t_p\right)\Bigg]\Bigg\}, \end{aligned} \quad (16)$$

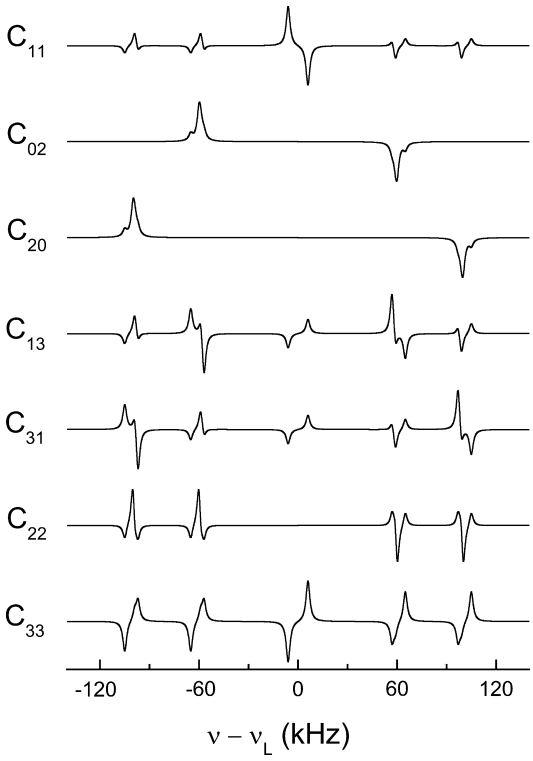

Fig. 3. Spectra $C_{ij}(\omega)$ associated with the tensor products $\hat{T}_{l_i 0}\hat{T}_{l_j 0}$ appearing in Eq. (14) for the following parameters: $\omega_{Qi} = 2\pi \times 100$ kHz, $\omega_{Qj} = 2\pi \times 60$ kHz and $\omega_D = 2\pi \times 1$ kHz. The peaks at a frequency ω' are shown as Lorentzian lines $\propto \Gamma/(4(\omega - \omega')^2 + \Gamma^2)$ with the dipolar broadening parameterized by $\Gamma = 2\pi \times 1.4$ kHz. The different spectra are shown for the same intensity-scale except for C_{02} and C_{20} which are divided by a factor of 10.

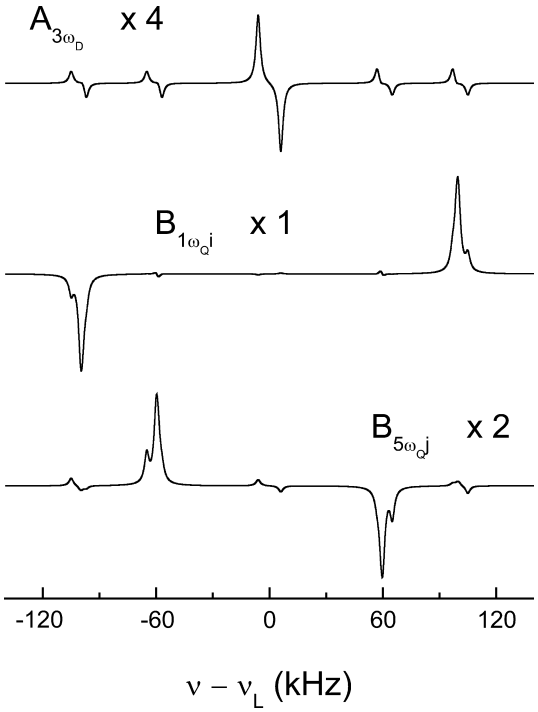

Fig. 4. Spectra $A(\omega)$ and $B(\omega)$ corresponding to the a and b coefficients appearing in Eq. (15). The parameters shown for the graphical representation are the same as used for Fig. 3 except for ω_D which was chosen to be $2\pi \times 2$ kHz. The use of larger still ω_D would only shift the dipolar peaks further away from the associated quadrupolar peaks or from the central part of the spectrum. This would lead to a multiplet appearance of the spectrum. Such a discrete splitting structure is then of course a consequence of the use of a unique dipolar coupling frequency ω_D. In a realistic situation there will be a distribution of couplings giving rise to a continuous dipolar broadening.

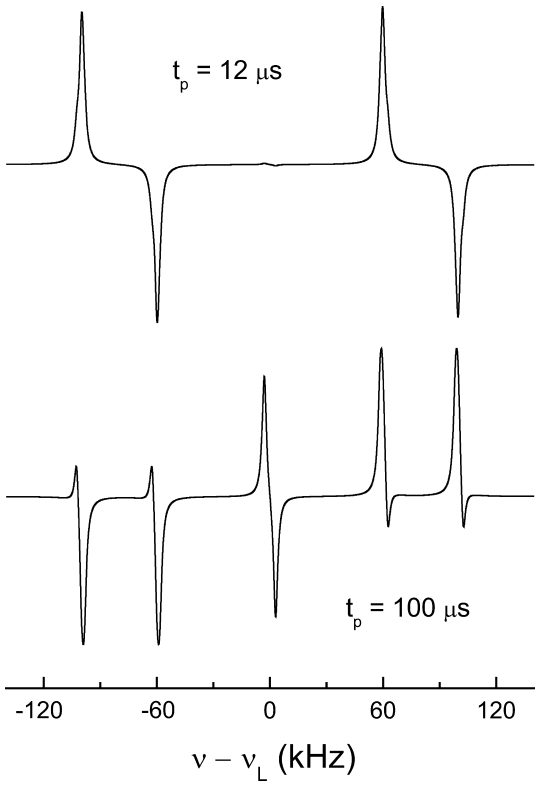

Fig. 5. Spin-alignment spectra $I(\omega)$ as calculated using Eq. (15) (A) for $t_p = 10\,\mu s$ and (B) for $t_p = 100\,\mu s$. For the parameters $\omega_{Qi} = 2\pi \times 100$ kHz, $\omega_{Qj} = 2\pi \times 60$ kHz, and $\omega_D = 2\pi \times 1$ kHz used in this plot, $a_{3\omega D}$ reaches its maximum at an evolution time of about $100\,\mu s$.

or the corresponding spectrum gives by far the largest contribution to the "central" feature, cf. Fig. 4.

According to Eq. (15) the stimulated-echo spectra for a given t_p are made up of a suitable superposition of the sub-spectra presented in Fig. 4. In Fig. 5 we show two spectra for a particular choice of quadrupolar and dipolar frequencies. The evolution times were chosen (a) small $t_p = 12\,\mu s$ and (b) such that for $\omega_D/2\pi = 1$ kHz the coefficient $a_{3\omega_D}$ is maximum. The maximum shows up at a time $t_p \approx 100\,\mu s$ (see also Fig. 6B) which is somewhat longer than corresponding to the first term in Eq. (16) alone. The coefficient $a_{3\omega_D}$ is maximum for $3\omega_D t_p = \pi/2$ or $t_p \approx 83\,\mu s$. In Fig. 5A it is seen that for small evolution times practically no central component appears and that all contributions exhibit the same phase. Fig. 5B reveals that the magnitude of the central line can become quite sizeable when compared to that of the satellite intensities. Furthermore, it should be noted that in powdered samples the quadrupolar intensity is spread across the entire range spanned by the coupling constant(s) while the central contributions all appear, and thus add up, close to the center of the frequency range. Another interesting feature is that while the satellites all share the same almost absorptive line shape, that of the central line looks purely dispersive.

If we assume $\omega_D \ll \omega_{Qi}, \omega_{Qj}$, which will be a reasonable approximation for many experimental cases, then the corresponding echo spectrum contains a central doublet. In the presence of a sufficient degree of line broadening, this doublet in fact may appear as a central *line*. Under the same conditions all other lines will be at or close to $\pm\omega_{Qi}$ and $\pm\omega_{Qj}$. Furthermore, in this limit all the time dependences of the a and b modulation factors will have the same general form as the sine functions at which they appear in Eq. (15) as pre-factors but with t replaced by t_p. For example, the coefficients b_{ω_Q} will be approximately proportional to $\sin\left(\left(\frac{\omega_D}{2} - \omega_Q\right)t_p\right)$.

2.2. Echo signals

By inserting into Eq. (15) the explicit expressions for the $a(t_p)$ and $b(t_p)$ coefficients one obtains a sum of products of the form $\sin\omega_1 t_p \sin\omega_2 t$. Analogous to the arguments presented above this product may be

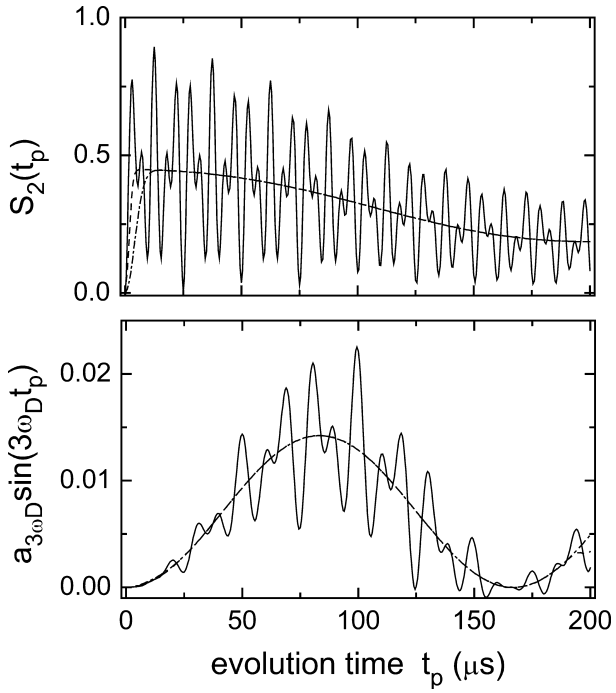

Fig. 6. (A) The total echo signal $S_2^{(i,j)}(t_p, t_m, t_p)$ as a function of t_p is represented by the solid line. It was computed according to Eq. (15) for $t_m \to 0$ and with the parameters used in Fig. 5. (B) The purely dipolar contribution $a_{3\omega_D}\sin(3t_p\omega_D)$ as given by the third term of Eq. (15) is represented as solid line. The dashed-dotted and the dashed lines represent powder averages as calculated using Eqs. (21) and (22) for variances $\sigma = 2\pi \times 20\,\mathrm{kHz}$ and $2\pi \times 50\,\mathrm{kHz}$, respectively.

decomposed into echo- and transient (anti-echo)-contributions. Different from the case of isolated spins the ''mixed'' terms such as

$$\begin{aligned}
&-\sin\left(\left(n\frac{\omega_D}{2}-\omega_Q\right)t_p\right)\sin(\omega_Q t)\\
&\quad=\frac{1}{2}\left(\cos\left(\left(-n\frac{\omega_D}{2}+\omega_Q\right)t_p-\omega_Q t\right)\right)\\
&\qquad-\frac{1}{2}\left(\cos\left(\left(-n\frac{\omega_D}{2}+\omega_Q\right)t_p+\omega_Q t\right)\right),
\end{aligned}\tag{17}$$

yield an echo for $t = \left(1 - n\frac{\omega_D}{2\omega_Q}\right)t_p$ with $n = +\frac{1}{2}, +\frac{3}{2}, -\frac{5}{2}$. For $\omega_D \ll \omega_Q$ this and all other combinations of modulation factors appearing in Eq. (15) reduce to the conventional echo condition $t \approx t_p$. It should be pointed out that taken together the cross terms, i.e., those involving the spins i and $j \neq i$ do not give rise to an echo. By consequently collecting all auto-correlation terms the total Jeener–Broekaert echo signal for the dipolar coupled spin-3/2 pair evolving under the approximated Hamiltonian, Eq. (13), is given by

$$\begin{aligned}
&S_2^{(i,j)}(t_p, t_m, t_p)\\
&\quad\approx\frac{9}{40}\sin\left(\omega_{Qi}(0)t_p\right)\sin(\omega_{Qi}(t_m)t_p)\\
&\qquad+\frac{9}{40}\sin(\omega_{Qj}(0)t_p)\sin(\omega_{Qj}(t_m)t_p)\\
&\qquad+\frac{73}{5120}\sin(3\omega_D(0)t_p)\sin(3\omega_D(t_m)t_p)\\
&\qquad+\frac{9}{80}\sin\left(\left(\frac{\omega_D}{2}-\omega_{Qi}\right)(0)t_p\right)\sin\left(\left(\frac{\omega_D}{2}-\omega_{Qi}\right)(t_m)t_p\right)\\
&\qquad+\frac{9}{80}\sin\left(\left(\frac{\omega_D}{2}-\omega_{Qj}\right)(0)t_p\right)\sin\left(\left(\frac{\omega_D}{2}-\omega_{Qj}\right)(t_m)t_p\right)\\
&\qquad+\frac{9}{160}\sin\left(\left(\frac{3\omega_D}{2}-\omega_{Qi}\right)(0)t_p\right)\\
&\qquad\times\sin\left(\left(\frac{3\omega_D}{2}-\omega_{Qi}\right)(t_m)t_p\right)\\
&\qquad+\frac{9}{160}\sin\left(\left(\frac{3\omega_D}{2}-\omega_{Qj}\right)(0)t_p\right)\\
&\qquad\times\sin\left(\left(\frac{3\omega_D}{2}-\omega_{Qj}\right)(t_m)t_p\right)\\
&\qquad+\frac{9}{160}\sin\left(\left(\frac{5\omega_D}{2}+\omega_{Qi}\right)(0)t_p\right)\\
&\qquad\times\sin\left(\left(\frac{5\omega_D}{2}+\omega_{Qi}\right)(t_m)t_p\right)\\
&\qquad+\frac{9}{160}\sin\left(\left(\frac{5\omega_D}{2}+\omega_{Qj}\right)(0)t_p\right)\\
&\qquad\times\sin\left(\left(\frac{5\omega_D}{2}+\omega_{Qj}\right)(t_m)t_p\right).
\end{aligned}\tag{18}$$

Thus the terms evolving predominantly under ω_{Qi} give rise to a pre-factor $\frac{9}{40}+\frac{9}{80}+\frac{9}{160}+\frac{9}{160}=\frac{9}{20}$ as is to be expected from a comparison with the result for isolated spins, Eq. (3). The same pre-factor stems of course from terms which involve ω_{Qj} so that the relative weight of the purely dipolar contribution

$$S_2^{(D)}(t_p, t_m, t_p) = \frac{73}{5120}\sin(3\omega_D(0)t_p)\sin(3\omega_D(t_m)t_p)\tag{19}$$

to the echo is only $\frac{73}{5120}/\frac{18}{20} \approx 1.6\%$.

Depending on the time interval(s) that are varied experimentally there are several ways to use the Jeener–Broekaert signal $S_2^{(i,j)}(t_p, t_m, t)$ to obtain information about the coupled quadrupolar spin pair. The dependence on the detection time t for fixed t_p and t_m yields one-dimensional spectra as discussed above, cf. Fig. 5. An additional systematic variation of the evolution time t_p forms the basis for the acquisition of two-dimensional spectra, a perspective that will not be pursued further in the present article.

Regarding the echo variant ($t = t_p$) of this experiment one can record the signal either as a function of the mixing time t_m for a chosen t_p or, alternatively, as a function of t_p for selected (usually very short) t_m. The

former echo experiment has been applied using a number of different probe nuclei for monitoring molecular, ionic, or atomic exchange processes [1] while the latter is useful for unraveling motional geometries [43] or for the separation of dipolar and quadrupolar contributions to the echo signal [8].

In Fig. 6 we present the calculated echo signals for variable t_p in conjunction with $t_m \to 0$. In frame (a) the full echo signal according to Eq. (15) is shown. The modulation in the signal is due to the presence of the quadrupolar frequencies, chosen as $\omega_{Qi} = 2\pi \times 100\,\text{kHz}$ and $\omega_{Qj} = 2\pi \times 60\,\text{kHz}$. The overall decay of the signal reflects the destructive interference of the various terms appearing in Eq. (15). The difference in the frequencies of these terms arises from the dipolar interaction. For the representation in Fig. 6A we have chosen $\omega_D = 2\pi \times 1\,\text{kHz}$. These results may be compared with the purely dipolar contribution shown in Fig. 6B. The built-up of the latter signal, as calculated using the third term in Eq. (15), cf. also Eq. (19), is slower as compared to the one seen in frame (a). This reflects the fact that the quadrupolar frequencies are assumed to be much larger than the dipolar one.

2.3. Spin triples and powder averages

The above computations only refer to *pairs* of spins. To obtain some insight into how the situation might change for larger spin systems, as a first step we have performed simulations for three quadrupolar spins that are mutually dipolarly coupled. Another way of considering the presence of a larger number of spins is to compute powder averages. This is done within the spin-pair approximation, further below.

The approximation leading to the simplified Hamiltonian $\hat{H}_{\text{app}}^{(i,j)}$, Eq. (13), can be extended to three spins (i,j,k). As the analytical calculations turned out to be cumbersome for this case, a simulation within the GAMMA [44] environment was performed. The quadrupolar frequencies of the three nuclei were chosen 20 kHz apart in order to avoid flip-flop transitions between the outer energy levels. The matrix elements of $\hat{H}_{\text{app}}^{(i,j,k)}$ were calculated by setting up a full Hamilton matrix considering quadrupolar and dipolar interactions as well as a second "reduced" matrix taking into account quadrupolar interactions, only. In a second step the matrix elements governing the flip-flop transitions between the inner energy levels were extracted from the full matrix and inserted into the "reduced" one. The matrix elements relevant for the flip-flop transitions are those between energy levels characterized by spin quantum numbers $m_\alpha = \pm\frac{1}{2}$ (with $\alpha = i,j,k$). The non-vanishing off-diagonal elements for $\alpha = i$ are of the form $\langle m_i, -\frac{1}{2}, +\frac{1}{2}|\hat{H}_{\text{app}}^{(i,j,k)}|m_i, +\frac{1}{2}, -\frac{1}{2}\rangle = \langle m_i, +\frac{1}{2}, -\frac{1}{2}|\hat{H}_{\text{app}}^{(i,j,k)}|m_i, -\frac{1}{2}, +\frac{1}{2}\rangle = -4\omega_D$ and analogously with m_j and m_k as the passive spin.

We generated the spectra $C_{ijk}(\omega)$ associated with the tensor products $\hat{T}_{l_i0}\hat{T}_{l_j0}\hat{T}_{l_k0}$ by taking the density matrix $\rho(t_p)$ after the second RF pulse as a function of t_p, forming the trace with the relevant 3-spin product operators, and performing a Fourier transformation with respect to t_p. Analogous to the 2-spin system, only product operators $\hat{T}_{l_i0}\hat{T}_{l_j0}\hat{T}_{l_k0}$ with *even* $l_i + l_j + l_k$ contribute to $\rho(t_p)$ when applying two out-of-phase pulses. The frequencies that occur are somewhat different from those calculated for the spin pair: while on the basis of Eq. (15) the modulation frequencies $\omega_Q + n\omega_D$ with $n = 0, -\frac{1}{2}, -\frac{3}{2}$, and $+\frac{5}{2}$ occur, for the spin triple $n = 0, -\frac{3}{2}$, and $+\frac{9}{2}$ can be inferred from plots of the spectra (not shown). For the central line, the dipolar interaction gives rise to a frequency of $\pm 6\omega_D$ for the 3-spin system instead of $\pm 3\omega_D$ for the 2-spin system.

From simulations using the full 3-spin Hamiltonian the central frequencies of $\pm 6\omega_D$ are confirmed. However, for the satellite frequencies we find $\omega_Q + n\omega_D$ with $n = 0, \pm 2, \pm 4, \pm 6$, i.e., with integer n similar to the full 2-spin system. From these computations we conjecture that for an N-spin system the central frequencies appear at $\pm 3(N-1)\omega_D$ and that $n \leqslant 3(N-1)$. This was confirmed from simulations of the full Hamiltonian also for $N = 4$.

In the following we will discuss the evolution time dependence of the echo intensity. Simulations using the approximate 3-spin approach revealed that the t_p dependences of the total echo signal and that of the purely dipolar contributions look similar to the ones presented in Fig. 6 (not shown). In detail, of course, the modulation pattern appears somewhat different.

The overall behavior is more clearly seen if one considers more and more additional modulation frequencies. This idea is most easily implemented by taking a powder average of Eq. (15). Using this equation we have computed $\langle S_2^{(i,j)}(t_p, t_m, t_p)\rangle$ as well as the contribution of the third term in this equation for fixed $t_m \to 0$ and variable t_p by employing a simple Gaussian distribution of quadrupolar frequencies. If the variance in the frequencies ω is denoted σ then one has to evaluate integrals of the type

$$\begin{aligned}\left\langle \sin\left[\left(\frac{n\omega_D}{2} \pm \omega\right)t_p\right]\right\rangle &= \int_{-\infty}^{\infty} \frac{1}{\sigma\sqrt{2\pi}} \exp\left(-\frac{\omega^2}{2\sigma^2}\right) \\ &\quad \times \sin\left[\left(\frac{n\omega_D}{2} \pm \omega\right)t_p\right] \mathrm{d}\omega \\ &= \exp\left(-\frac{1}{2}\sigma^2 t_p^2\right) \sin\left(\frac{n}{2}\omega_D t_p\right).\end{aligned} \tag{20}$$

For the third term of Eq. (15) this simple averaging procedure yields

$$\langle a_{3\omega_D}\sin(3\omega_D t_p)\rangle = \frac{\sin(3\omega_D t_p)}{20,480}\left\{292\sin(3\omega_D t_p) + 6\left[-5\sin\left(\frac{\omega_D}{2}t_p\right) + 22\sin\left(\frac{3\omega_D}{2}t_p\right) + 17\sin\left(\frac{5\omega_D}{2}t_p\right)\right]\exp\left(-\frac{1}{2}\sigma^2 t_p^2\right)\right\}. \quad (21)$$

To compare the computations directly with the ones shown in Fig. 6 we set $\omega_D = 2\pi \times 1\,\text{kHz}$ and $\sigma = 2\pi \times 20\,\text{kHz}$ as well as $2\pi \times 50\,\text{kHz}$. For all cases the build-up of the signal for small evolution times is proportional to the square of t_p. Depending on σ, the damping of the already relatively small terms in the square brackets is practically complete after about 10–15 μs. Similarly the treatment of the other terms in Eq. (15) gives results that can be written as a sum of a contribution S_0 which does not depend on σ and other contributions which do. Since, as a function of t_p, these latter contributions are quickly damped away, here we focus again on the first contribution which is

$$S_0(t_p) = \frac{1}{40,960}(7519 + 4320c_1 + 1098c_2 + 2160c_3 + 2160c_5 + 1125c_6 + 342c_8 - 292c_{12}). \quad (22)$$

Here we used the abbreviation $c_n = \cos(n\omega_D t_p/2)$. In the limit $\omega_D \to 0$ or $t_p \to 0$ this expression gives $S_0 \to 9/20$, as it should. The solid line in Fig. 6 reflects Eq. (22) again with $\omega_D = 2\pi \times 1\,\text{kHz}$. While these averages nicely illustrate the overall behavior of the simple two-spin model one should also bear in mind that the averaging procedure itself is somewhat particular: in our computation it is implicitly assumed that the two quadrupolar and the dipolar frequencies are statistically independent from one another. This may not be the case in practice.

3. Stimulated-echo spectroscopy of β-eucryptite

The ^{7}Li NMR experiments were conducted at 46 and 127 MHz using a home-built spectrometer. Typical $\pi/2$ pulse lengths were in the range from 1.6 to 4 μs and allowed for a non-selective excitation of the entire spectrum. All spectra shown in this article were obtained by taking the Fourier transform of the measured signal starting from the relevant Jeener–Broekaert echo or solid-echo maximum. Spin–lattice relaxation times were measured using the inversion recovery solid-echo technique.

The β-eucryptite single crystals used in this study were grown from a LiF/AlF_3 flux. The synthesis and the detailed growth procedures have been described in [45]. For some experiments the crystals were aligned with the crystallographic c axis oriented perpendicular to the external magnetic field. First we will focus on experiments carried out at 127 MHz.

3.1. Spectra

For the measurements shown in Fig. 7 the crystal was rotated within the coil until the absorption lines were relatively well separated from one another. In that figure we compare a solid-echo spectrum with one recorded using the Jeener–Broekaert sequence. Both spectra exhibit six quadrupole-shifted pairs of lines as expected on the basis of the crystal structure. It is evident that the relative weight of the integrated satellite intensity of the spin-alignment spectrum is much larger than it is for the solid-echo spectrum. But, similar to what was observed previously for powdered Li ion conductors [8], the central line is still clearly visible in the spin-alignment spectrum. In accord with the calculations carried out in the previous section, this signals the presence of significant homonuclear interactions among the ^{7}Li nuclei. The full widths at half maximum of the central and of the satellite peaks are $4.5 \pm 0.6\,\text{kHz}$ and these widths agree within experimental error. For temperatures at and below ambient in a previous study the widths of the central line were reported to be between 4.5 and 6 kHz, depending on the orientation of the crystal relative to the magnetic field [25]. This dipolar line width roughly agrees with estimates for a finite linear chain of ^{7}Li-spins separated by 3.7 Å [25].

3.2. Dependence on the evolution time

The fraction of the integrated quadrupolar intensity relative to the total spectral intensity depends on the

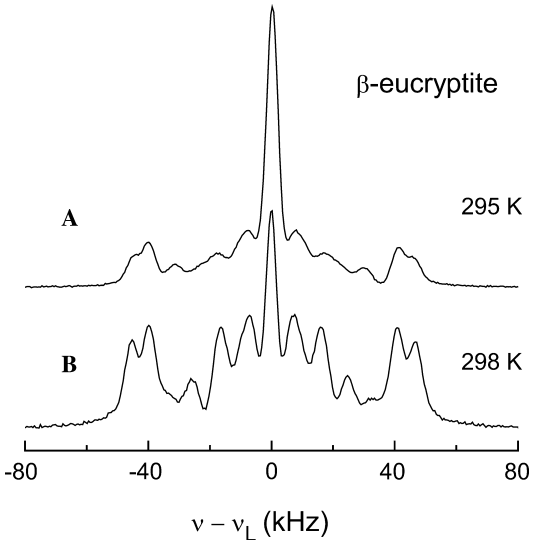

Fig. 7. (A) Solid-echo spectrum of a single crystal of β-eucryptite. The pulse delay was set to 20 μs. (B) Spin-alignment spectrum recorded with $t_p = 12\,\mu\text{s}$ and $t_m = 10\,\text{ms}$. Both spectra were taken at 127 MHz.

evolution time t_p since each satellite contribution to the Jeener–Broekaert spectrum at a frequency ω_k is expected to be modulated by $|\sin \omega_k t_p|$. This has been demonstrated previously for ^{9}Be, another spin-3/2 probe that can be excited non-selectively in the solid state [8]. The expectation regarding the harmonic modulation can be tested for β-eucryptite by measuring the ^{7}Li spin-alignment spectra and thus the intensities of the satellite peaks as a function of t_p. Some experimentally determined intensities are shown in Fig. 8. They were obtained by fitting a superposition of Gaussian functions to the experimental spectra. At least the behavior of the outer satellites is compatible with a $|\sin \omega_k t_p|$ dependence which is indicated by the solid lines. Here $\pm\omega_k$ was taken from the positions of the peaks evident from Fig. 7. Furthermore, the lines plotted in Fig. 8 were left-shifted by 4 μs, thus taking into account the evolution during the RF pulses on a phenomenological basis. For the inner satellites the agreement is less satisfactory either because the absolute intensities are smaller or, due to interference with the adjacent lines, the quadrupolar frequencies could not reliably be determined.

However, it is clear from Fig. 8 that also the outer lines fail to follow a strict $|\sin \omega_k t_p|$ dependence for longer t_p. This can qualitatively be understood with reference to Eq. (15). There one recognizes that several discrete frequencies close to ω_Q appear which span a range $\Delta\omega_D = \left|-\frac{5}{2} - \left(+\frac{3}{2}\right)\right|\omega_D = 4\omega_D$ given by the deviation from the dominant quadrupolar modulation frequency. Thus a dipolar coupling of $\omega_D = 2\pi \times 1$ kHz in the representation of Fig. 8 will lead to a dephasing on a time scale of about $t \approx 1/(\Delta\omega_D) = 1/4 \times 2\pi \times 1$ kHz) ≈ 40 μs. It is clear that the consideration of coupled ^{7}Li *pairs* presents an oversimplification with respect to the situation in β-eucryptite. Nevertheless it may be helpful to rationalize the relatively rapid damping of the oscillations seen in Fig. 8 in the presence of dipolar couplings.

In Fig. 9 the central and the integrated satellite intensities for β-eucryptite are plotted in a large range of effective evolution times $t_{p,eff} = t_p + 4$ μs. Thus in addition to the nominal times the evolution of the spin system during the RF pulses is approximately taken into account. The integrated satellite intensity is more or less fully developed already at the smallest accessible evolution times, as expected on the basis of their large coupling constants [4]. The central intensity, on the other hand, smoothly evolves, reaches a maximum only near 100 μs and then decays. In a properly scaled representation of the data (not shown) one can see that the transversal decays of the central and of the satellite contributions proceed on the same time scale. Thus the evolution of the echo intensity qualitatively agrees with that shown in Fig. 6.

The type of information thus obtained from Fig. 9 is similar to that extracted from stimulated-echo measurements using polycrystalline samples [8]. From Eq. (18) it is clear that dipolar and quadrupolar contributions are both contained in the echo signal. Therefore, in our previous study we have detected the "central" components by recording the intensity of the pedestal rather than that of the echo. Dipolar and quadrupolar contributions can then only be separated by a subtraction procedure. In this respect experiments using single crystals facilitate a simpler separation.

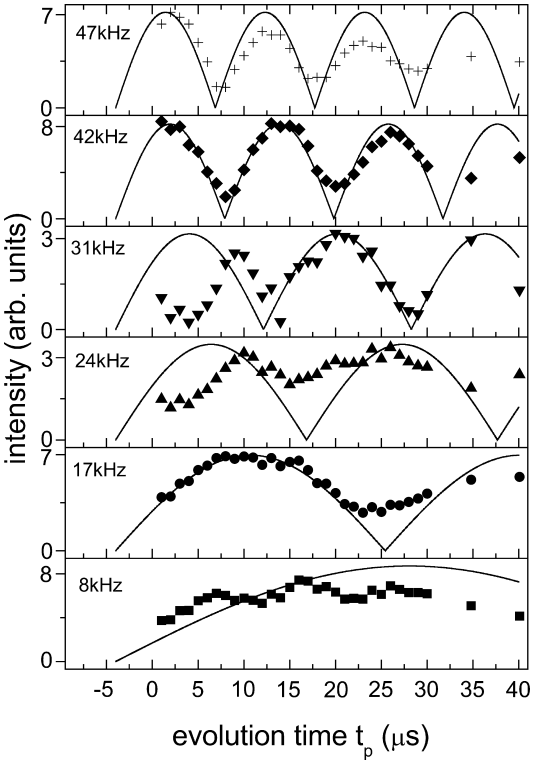

Fig. 8. Satellite intensities of β-eucryptite as a function of the evolution time for a fixed, short mixing time $t_m = 50$ μs. The solid lines represent a $|\sin \omega_k t_p|$ dependence with ω_k given by the quadrupolar frequencies apparent from Fig. 7. To account for the finite pulse length the lines are left-shifted by 4 μs.

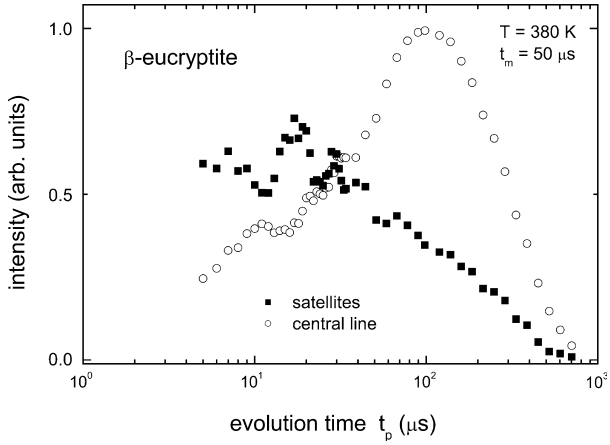

Fig. 9. Evolution time dependent integrated intensity of the central line and of the satellites for a mixing time of $t_m = 50$ μs. The data are right-shifted by 4 μs.

3.3. Dependence on the mixing time

To detect slow processes one may vary the mixing times systematically. We have recorded spin-alignment spectra for fixed evolution times as a function of t_m. In Fig. 10, we present the mixing-time dependent intensities of the central and of the satellite peaks acquired at $T = 380$ K. It is seen that within a factor of two all satellite peaks decay on the same time scale. The central peak decays somewhat faster. For comparison purposes we also include the mixing time dependence of the echo signal recorded under otherwise identical conditions. It is seen that the echo signal decays to zero. It can be described by a stretched exponential function

$$S_2(t_m) = M \exp[-(t_m/\tau_1)^{\beta_1}], \tag{23}$$

with an amplitude M, a time constant $\tau_1 = 0.057$ s, and a stretching exponent $\beta_1 = 0.54$.

If the echo decay is due to Li^+ ion exchange processes then one would expect that a plateau value of $Z = 1/N$ is reached if there exist $N = 6$ magnetically inequivalent, equally populated sites or, in other terms, if six equilibrium quadrupole-perturbed frequency pairs $\pm\omega_k$ are present. We have seen that for the coupled pair additional frequencies exist, see, e.g., Eq. (15), which could reduce Z to a value smaller than $1/N$. Beyond the spin pair-approximation one may thus expect that Z is the closer to zero the more spins are effectively coupled. We do not believe that the complete decay of the echo function is due to that of the longitudinal states used to store the information during the mixing time. Such a decay will certainly be governed by T_{1Q}, the spin–relaxation time associated with the decay of quadrupolar spin order. Except for specially selected crystal orientations T_{1Q} and the spin–lattice relaxation time T_1 are expected to be very similar [19]. In β-eucryptite T_1 is between 8 and 10 s at $T \approx 380$ K, depending on the orientation of the sample. However, from measurements carried out at several crystal orientations it is found that neither T_1 [24] nor the significantly faster alignment decay show a significant orientation dependence see also Fig. 12, below.

To unambiguously interpret the data shown in Fig. 10 in terms of ionic exchange one would expect a transfer of intensity among the peaks corresponding to connected Li^+ sites. Since at the evolution time relevant for Fig. 10 the initial ($t_m \to 0$) intensities are not all equally large (cf. Fig. 8), this implies that one or more peaks should become stronger with increasing mixing time. This was not observed.

Before discussing these issues further let us note that similar results were obtained for other evolution times at $T = 380$ K. Additional spin-alignment echo decays were recorded for lower temperatures and, up to this point, employing a Larmor frequency of 127 MHz. To investigate also higher temperatures a probe tuned to 46 MHz was available. Due to the limited sample space available in that probe only small single crystals could be used. Their exact orientation was not recorded and only echo experiments were carried out.

Spin-alignment echo decays at various temperatures are shown in Fig. 11 together with fits using a two-step function characterized by the amplitudes M_1 and M_2 according to

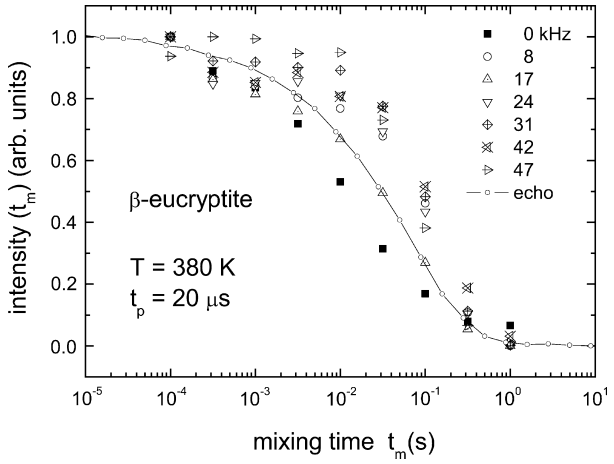

Fig. 10. Spin-alignment decay of β-eucryptite. The symbols represent the normalized intensities of the central line and of the satellites as a function of the mixing time for a fixed evolution time of $t_p = 20$ μs. The connected dots show the decay of the *echo* intensity. The measurements were taken at 127 MHz.

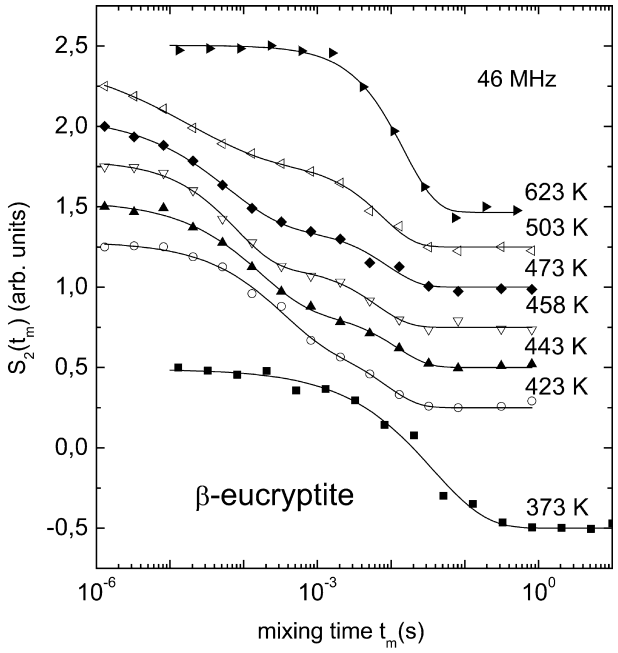

Fig. 11. Mixing time dependent spin-alignment echo decays recorded at 46 MHz. For the sake of clarity the data acquired at 373 K were shifted downwards by 0.5, those at 423, 443 K, etc., upwards by 0.25, 0.5, etc. For the measurements the evolution time was set to 10 μs. The lines are fits using Eq. (24).

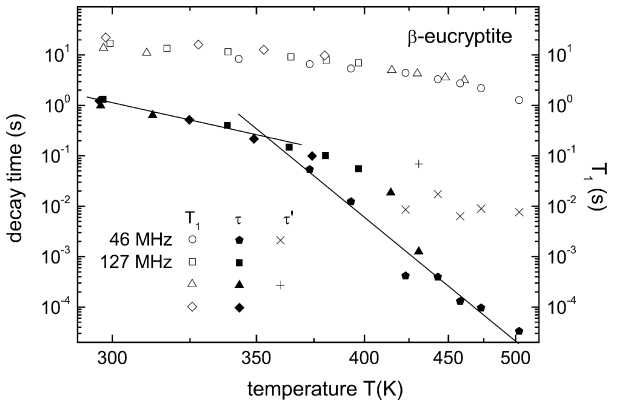

Fig. 12. Spin-alignment echo decay times (full symbols) and spin–lattice relaxation times (open symbols) measured for two different Larmor frequencies. For 127 MHz the different symbols correspond to different unspecified orientations of the crystal. The solid lines correspond to thermally activated behaviors with energy barriers of 0.27 eV (lower temperatures) and 0.94 eV (higher temperatures).

$$S_2(t_m) = M_1 \exp[-(t_m/\tau_1)^{\beta_1}] + M_2 \exp[-(t_m/\tau_2)^{\beta_2}]. \quad (24)$$

Here the time constants τ_1 and τ_2 describe the decay at longer and at shorter times, respectively. The decay at longer times proceeds almost exponentially. The faster decay is thermally activated and stretched with $\beta_2 \approx 0.65 \pm 0.1$. The relative weight of the faster decay decreases almost linearly for $373\,\mathrm{K} < T < 623\,\mathrm{K}$.

4. Discussion

The time constants from fits to the data presented in Fig. 11 are shown in Fig. 12. Also included in this plot are fits to the spin-alignment decays monitored at 127 MHz and from our measurements of the spin–lattice relaxation times of β-eucryptite. These data were recorded for two Larmor frequencies and for differently oriented crystals, but the results coincide within experimental error. The same is true for the time constants τ_1 and τ_2 employed to describe the decay of the spin-alignment echoes. These coincidences preclude a clear-cut separation of decays due to ionic hopping processes from those that potentially can arise from longitudinal spin-relaxation processes. In our previous study of other Li ion conductors the latter could clearly be recognized from their dependence on the Larmor frequency [8].

The temperature dependence of the time constant τ_1 of the spin-alignment decay is similar to that of T_1, at least for $T < 350\,\mathrm{K}$. However, the short-time constant τ_2 showing up for $T > 350\,\mathrm{K}$ exhibits a more pronounced temperature dependence. The fast-time decays shown in Fig. 11 proceed on a time scale which are not much longer than the evolution time of 10 μs and in a time regime in which also spin–spin relaxation could take place. A priori it is of course not clear whether a dipolarly induced violation of coherence pathways leads to the observation of T_2 effects. Such effects would be eliminated by the phase cycle employed in the present work if the dipolar interactions could be neglected. However, the fact that the time constants describing the fast-time decays are in line with the much longer time constants appearing at much lower temperatures makes an interpretation in terms of T_2 effects rather unlikely. In this context we should note that for other crystalline Li^+ ion conductors we have found that the transversal decay observed using Jeener–Broekaert spectroscopy is complete within less than a few ms [8]. Additionally we found that the decay times show a well-defined and smooth evolution according to an Arrhenius law over a dynamic range of more than three decades including decay times much smaller than 1 ms [8].

The solid lines in Fig. 12 represent thermally activated behaviors according to $\tau_{1,2} \propto \exp[E_{1,2}/(k_B T)]$ with energy barriers $E_1 = (0.27 \pm 0.03)\,\mathrm{eV}$ (lower temperatures) and $E_2 = (0.94 \pm 0.10)\,\mathrm{eV}$ (higher temperatures). Thus E_2 is slightly larger than the energy barrier of about 0.8 eV as measured using spin–lattice relaxometry, see, e.g. [21], and conductivity spectroscopy, see, e.g. [31]. The numerical value of the energy barrier E_1 agrees with that inferred from the temperature dependence of the width of the central line of β-eucryptite [25]. In this context it may be interesting to note that from a recent density functional calculation of this crystal it has been reported that the energy barrier for uncorrelated Li^+ hopping (somewhat larger than 0.8 eV) is considerably larger than the energy barrier for correlated Li^+ motions (about 0.3 eV per ion) [29]. From diffuse neutron scattering of β-eucryptite it has been inferred that 19 ± 3 Li^+ ions participate in this correlated motion [28], so that the total energy barrier for this process is much larger than for the uncorrelated motion. The fact that we observe the energy barrier *per ion* suggests that the spin-alignment experiment acts predominantly as a single-particle probe of the dynamics.

5. Conclusions

To summarize, in this article we have treated the evolution of spin-3/2 nuclei in solid-like environments taking into account quadrupolar *and* dipolar interactions. The latter was done in a simple approximation focusing mostly on spin pairs and in particular on the flip-flop term which connects the central transitions of the two coupled nuclei. At first glance, the consideration of spin pairs may appear somewhat artificial unless one considers specific molecules (for ^2H pairs, see, e.g. [46]) or, in connection with spin-3/2 systems, one first employs a 6-quantum filter [47].

The simple approach adopted in the present article reveals several interesting results. Most important is the

theoretical finding that in the spin-alignment spectra of coupled ^{7}Li nuclei a central component will show up. Also we have found that the apparent phase of this component can differ from that of the satellite contributions. Simulations have shown that these results are not significantly altered for the case of spin triples. The relative amplitudes of the pure quadrupolar, of the pure dipolar, and of the mixed contributions to the alignment-echo amplitudes were discussed for cases applicable to single crystals and powders. We also briefly discussed relaxation effects. The evolution time dependence of the calculated echo signal demonstrates, how the dipolar and the quadrupolar contributions can effectively be separated by a suitable choice of t_p.

For the experimental part of this work we investigated single crystals of β-eucryptite, mostly using the stimulated-echo sequence. In the corresponding spectra a central line appears albeit with an intensity which is much smaller than in the solid-echo spectra. Differences in the time scales governing the build-up and the decay of the central and satellite lines were demonstrated via a systematic variation of the evolution time t_p. As a function of the mixing time t_m the two types of lines exhibit similar decay times with the central line vanishing slightly faster than the satellites typically do. This finding is consistent with the notion that the purely dipolar (i.e., central) decay is governed by the hopping of at least two Li^+ ions, see also Fig. 10 in [8]. The two-particle processes should always be somewhat faster than the ones which are dominated by single-ion jumps.

Finally, from temperature dependent measurements as a function of the mixing time we were able to map out energy barriers that are consistent with those for the uncorrelated Li^+ hopping as well as for the correlated Li^+ motions. At higher temperatures a two-step behavior was found for the decay of the stimulated echo. While its short-time decay could unambiguously be assigned to the Li^+ ion hopping, we discussed several interpretations for the slower one.

Acknowledgments

The Deutsche Forschungsgemeinschaft supported this project under Grant No. Bo1301/5 and within the Graduiertenkolleg 298.

References

[1] K. Schmidt-Rohr, H.W. Spiess, Multidimensional Solid-State NMR and Polymers, Academic Press, London, 1994.
[2] E. Göbel, W. Müller-Warmuth, H. Olyschläger, H. Dutz, J. Magn. Reson. 36 (1979) 371.
[3] X.-P. Tang, Y. Wu, J. Magn. Reson. 133 (1998) 155.
[4] R. Böhmer, J. Magn. Reson. 147 (2000) 78.
[5] J. Jeener, P. Broekaert, Phys. Rev. 157 (1967) 232.
[6] X.-P. Tang, R. Busch, W.L. Johnson, Y. Wu, Phys. Rev. Lett. 81 (1998) 5358.
[7] R. Böhmer, T. Jörg, F. Qi, A. Titze, Chem. Phys. Lett. 316 (2000) 417.
[8] F. Qi, T. Jörg, R. Böhmer, Solid State Nucl. Magn. Reson. 22 (2002) 484.
[9] M. Vogel, Phys. Rev. B 68 (2003) 184301.
[10] M. Wagemaker, A.P.M. Kentgens, F.M. Mulder, Nature 418 (2002) 397.
[11] V.W.J. Verhoeven, I.M. De Schepper, G. Nachtegaal, A.P.M. Kentgens, E.M. Kelder, J. Schoonman, F.M. Mulder, Phys. Rev. Lett. 86 (2001) 4314.
[12] S. Wi, L. Frydman, J. Chem. Phys. 112 (2000) 3248.
[13] J. Jeener, Adv. Magn. Reson. 3 (1968) 205.
[14] R.R. Ernst, G. Bodenhausen, A. Wokaun, Principles of Nuclear Magnetic Resonance in One and Two Dimensions, Clarendon, Oxford, 1987.
[15] N. Boden, P.K. Kahol, Mol. Phys. 40 (1980) 1117.
[16] C. Müller, S. Idziak, N. Pislewski, U. Haeberlen, J. Magn. Reson. 47 (1982) 227.
[17] G. Diezemann, J. Chem. Phys. 103 (1995) 6368.
[18] G. Diezemann, H. Sillescu, J. Chem. Phys. 103 (1995) 6385.
[19] A. Müller, H. Zimmermann, U. Haeberlen, J. Magn. Reson. 126 (1997) 66.
[20] H.T. Weaver, R.M. Biefeld, Solid State Commun. 18 (1976) 39.
[21] J.B. Boyce, J.C. Mikkelsen Jr, B.A. Huberman, Solid State Commun. 29 (1979) 507.
[22] D.M. Follstaedt, P.M. Richards, Phys. Rev. Lett. 37 (1976) 1571.
[23] D. Brinkmann, in: B.V.R. Chowdhari et al. (Eds.), Solid State Ionics: Science and Technology, World Scientific, Bangalore, 1998, pp. 93–102.
[24] D. Brinkmann, M. Mali, J. Roos, E. Schweickert, Solid State Ionics 5 (1981) 433.
[25] E. Schweickert, M. Mali, J. Roos, D. Brinkmann, P.M. Richards, R.M. Biefeld, Solid State Ionics 9 and 10 (1983) 1317.
[26] V. Tscherry, H. Schulz, F. Laves, Z. Kristallogr. 135 (1972) 161.
[27] H. Guth, G. Heger, in: P. Vashishta, J.N. Mundy, G.K. Shenoy (Eds.), Fast Ion Transport in Solids, Electrodes and Electrolytes, Elsevier, North-Holland, 1979, p. 499.
[28] W. Press, B. Renker, H. Schulz, H. Böhm, Phys. Rev. B 21 (1980) 1250.
[29] A.I. Lichtenstein, R.O. Jones, H. Xu, P.J. Heaney, Phys. Rev. B 58 (1998) 6219.
[30] L. Cormier, P.H. Gaskell, G. Calas, J. Zhao, A.K. Soper, Phys. Rev. B 57 (1998) R8067.
[31] H. Böhm, Phys. Stat. Solidi A 30 (1975) 531.
[32] U.V. Alpen, E. Schönherr, H. Schulz, G.H. Talat, Electrochim. Acta 22 (1977) 805.
[33] G. Roth, H. Böhm, Solid State Ionics 22 (1987) 253.
[34] B. Munro, M. Schrader, P. Heitjans, Ber. Bunsenges. Phys. Chem. 96 (1992) 1718.
[35] R. Böhmer, M. Lotze, P. Lunkenheimer, F. Drexler, G. Gerhard, A. Loidl, J. Non-Cryst. Solids 172–174 (1994) 1270.
[36] Low Thermal Expansion Glass Ceramics, in: H. Bach, Schott Series on Glass and Glass Ceramics, Springer, Berlin, 1995.
[37] N. Müller, G. Bodenhausen, R.R. Ernst, J. Magn. Reson. 75 (1987) 297.
[38] G.D. Bowden, W.D. Hutchison, J. Khachan, J. Magn. Reson. 67 (1986) 415.
[39] B.C. Gerstein, C.R. Dybowski, Transient Techniques in NMR of Solids: An Introduction to Theory and Practice, Academic Press, Orlando, 1985, p. 130.
[40] F. Qi, Dissertation, Universität Mainz, 2003.
[41] G. Jaccard, S. Wimperis, G. Bodenhausen, J. Chem. Phys. 85 (1986) 6282.
[42] J.R.C. van der Maarel, Chem. Phys. Lett. 155 (1989) 288.

[43] R. Böhmer, G. Diezemann, G. Hinze, E. Rössler, Prog. NMR Spectrosc. 39 (2001) 191.
[44] S.A. Smith, T.O. Levante, B.H. Meier, R.R. Ernst, J. Magn. Reson. 106a (1994) 75.
[45] S. Haussühl, W. Nagel, H. Böhm, Z. Kristallogr. 169 (1984) 299.
[46] G. Facey, D. Gusev, R.H. Morris, S. Macholl, G. Buntkowsky, Phys. Chem. Chem. Phys. 2 (2000) 935.
[47] M.J. Duer, A.J. Painter, Chem. Phys. Lett. 313 (1999) 763.